Progress In Electromagnetics Research C, Vol. 173, 215–229, 2026

PIER C

(Received 18 June 2026, Accepted 13 August 2026, Scheduled 13 September 2026)

CMA-Based Design of a Wideband RHCP Antenna with Gain and Bandwidth Enhancement Using Parasitic Element

Sagar B. Pokharkar[1,*] and Kanchan Tiwari[2]

[1]*Department of Electronics & Telecommunucation*
AISSMS Institute of Information Technology, Savitribai Phule Pune University, Pune, India
[2]*Department of Electronics & Telecommunucation*
MES Wadia College of Engg, Savitribai Phule, Pune University, India

ABSTRACT: Existing wideband circularly polarized (CP) antennas generally face trade-offs among wide impedance bandwidth, broad axial ratio (AXR) bandwidth, gain, and compactness in single-layer implementation. Furthermore, a number of reported designs are multi-layer or metasurface-based or require complex feeding networks, making them more complex to manufacture, resulting in increased fabrication costs. In this paper, we develop a wideband circularly polarized (CP) antenna design using an active central patch with four parasitic patches on an FR4 substrate. The CP condition is obtained by exciting two orthogonal modes of equal magnitude and 90° phase difference, which are attained by perturbing the active patch and placing a diagonal coaxial feed on it. We enhance the broadside gain and bandwidth by loading parasitic patches around the active patch via electromagnetic coupling. This type of coupling improves aperture efficiency, impedance matching, and axial ratio bandwidth (ARBW). Characteristic Mode Analysis (CMA) is used to determine and optimize the dominant orthogonal modes responsible for circular polarization and radiation enhancement. The fabricated prototype shows a measured -10 dB impedance bandwidth (IBW) of 18.12% (5.42–6.50 GHz), an axial ratio bandwidth (ARBW) of 17.87% (5.35–6.40 GHz), and a broadside gain of 8.5 dBi. The measured and simulated results show excellent agreement, confirming the functionality of the designed antenna. The antenna's compact size, wide bandwidth, and high broadside gain make it a potential solution for broadband wireless communication, satellite-based systems, and C-band antenna applications.

1. INTRODUCTION

Circularly polarized (CP) antennas have been a subject of major consideration in recent years they can effectively mitigate multipath fading and polarization mismatch losses and preserve stable communication links irrespective of the relative orientation of the transmitter and receiver [1, 2]. In contrast to linearly polarized antennas, CP antennas emit rotating polarization electromagnetic fields, which allow antennas to receive strong signals despite complex propagation conditions. It makes them best suited to contemporary wireless networks: satellite communication, wireless sensing, IoT devices, radar systems, and 5G sub-6 GHz networks where polarization diversity and link reliability are key considerations [1–3]. One of the most promising frequency bands in these applications is the C-band (4.87 GHz), which provides a trade-off between long-range propagation, coverage, and high data-rate transmission. CP antennas used in this band find applications in satellite downlink, airborne communication, broadband wireless access (WiMAX, WLAN), and point-to-point backhaul systems [4].

Circularly polarized (CP) antennas have been the subject of much research interest because they reduce the effect of polarization mismatch, multi-path fading, and orientation sensitivity in current wireless communication systems. As a result, CP antennas are widely used in satellite communication, wireless sensor networks, radar, Internet of Things (IoT), and sub-6 GHz 5G wireless applications. The growing need for high data rate and reliable communication systems has resulted in a wide variety of techniques proposed to increase impedance bandwidth (IBW), axial ratio bandwidth (ARBW), radiation efficiency, and gain using optimized radiator geometries, feeding mechanisms, and parasitic loading techniques. Among them, parasitic-element loading is the most popular method to improve radiation performance and polarization stability via electromagnetic coupling. For instance, a C-band ring-shaped parasitic array, designed to achieve better radiation characteristics, did not produce stable broadside radiation but instead produced conical beam patterns [5]. Likewise, single- and dual-layer parasitic configurations were used to enhance impedance matching and broadside radiation of single-layer parasitic structures [2] and triangular coplanar parasitic elements for S-band applications [6, 7]. Recently, a few CP antennas have been developed using stacked slot-coupled structures, metamaterial-loaded radiators, shared cross-slot aperture structures with air gaps, and parasitic discs. While these techniques can achieve acceptable performance, they generally require multilayer structures, hybrid couplers, air gaps, or complex feeding networks, increasing fabrication complexity, antenna profile, and manufacturing cost [8, 9–12]. Other approaches to enhance antenna performance include using metasurfaces, reactive impedance surfaces (RISs), artificial ground structures (AGSs), defected ground

* Corresponding author: Sagar Babanrao Pokharkar (sagar.pokharkar@aissmsioit.org).

doi:10.2528/PIERC26061802

Published by THE ELECTROMAGNETIC ACADEMY

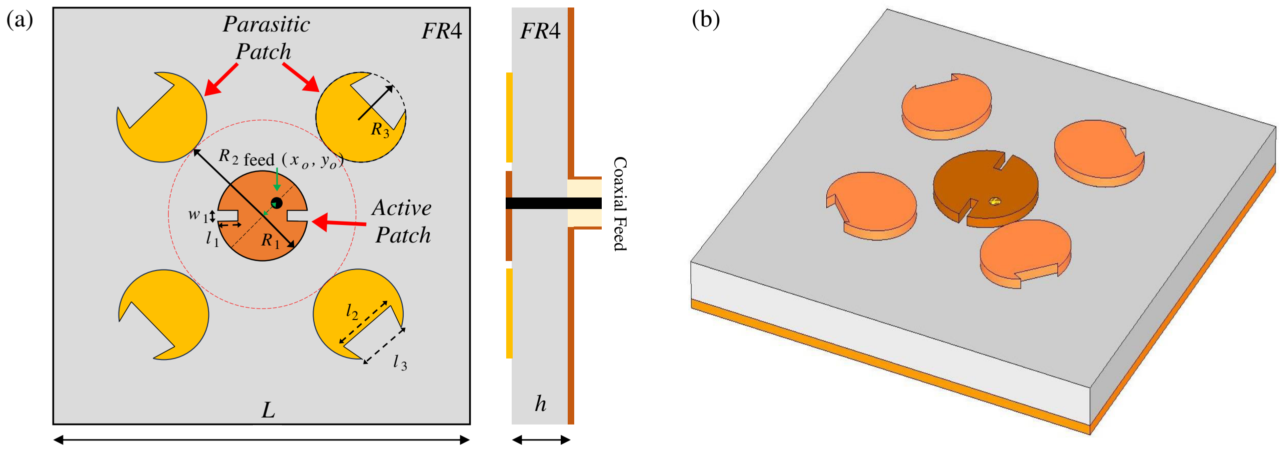

FIGURE 1. Design structure of the proposed antenna: (a) 2D view and (b) 3D view.

structures (DGSs), and metamaterial-inspired radiators [13–20]. Recently, some single-layer wideband monopole antennas with asymmetric meandered monopoles, slanted-edge DGS, and defected ground planes [8–12] have demonstrated excellent impedance bandwidth. However, these antennas are generally linearly polarized or have bidirectional radiation patterns, making them unsuitable for applications requiring stable broadside circular polarization. Moreover, recently reported CP antennas designed to achieve high gain and wide bandwidth often suffer from increased design complexity and fabrication difficulties. Despite several recent publications using Characteristic Mode Analysis (CMA) to explain modal behavior and circular polarization mechanisms, only a limited number of studies have used CMA as a systematic design methodology to simultaneously optimize orthogonal characteristic modes and parasitic electromagnetic coupling.

The proposed antenna adopts a Characteristic Mode Analysis (CMA)-based design methodology that systematically characterizes and excites orthogonal degenerate characteristic modes to achieve circular polarization. The antenna is implemented on a compact single-layer FR4 substrate, consisting of a slot-loaded circular active patch surrounded by four symmetrically arranged parasitic patches. The slot perturbation and diagonally positioned coaxial feed excite two orthogonal characteristic modes with nearly equal amplitude and a 90° phase difference, thereby generating stable right-hand circular polarization (RHCP). The proposed CMA-guided parasitic coupling mechanism enables a compact, low-cost, single-layer configuration with enhanced aperture efficiency, electromagnetic coupling, impedance matching, axial ratio bandwidth, and broadside gain, without requiring multilayer structures, metasurfaces, air gaps, or complex feeding networks as reported in recent studies. The fabricated prototype achieves a measured impedance bandwidth of 18.12% (5.42–6.50 GHz), a peak broadside gain of 8.5 dBi, and a 3 dB axial ratio bandwidth of 17.87% (5.35–6.40 GHz). The primary novelty of this work lies in systematically integrating Characteristic Mode Analysis with parasitic electromagnetic coupling, which enables simultaneous optimization of orthogonal characteristic modes to enhance impedance bandwidth, circular polarization performance, and radiation characteristics without multilayer structures, air gaps, metasurfaces, or hybrid feeding networks.

2. DESIGN WIDE-BAND CIRCULARLY POLARIZED ANTENNA

2.1. Designing Proposed Antenna Structure

Figure 1(a) displays the antenna's top and side views. The diagonal excitation of the central active patch is achieved via a coaxial probe feed at (x_0, y_0) to excite the orthogonal modes required for circular polarization. To satisfy the CP condition, a slot is etched on the active patch, generating two orthogonal modes of equal amplitude with a 90° phase difference. The parasitic patches have the same shape as the active patch, and four such patches are symmetrically arranged around it. The optimized spacing between active and parasitic patches provides strong electromagnetic coupling, enhancing impedance matching, aperture efficiency, and axial ratio bandwidth (ARBW). The side view illustrates the antenna configuration on an FR4 substrate of thickness h, highlighting the coaxial feed connection between the ground plane and the active patch. Fig. 1(b) presents the antenna's 3D perspective view, showing the spatial arrangement of active and parasitic patches and illustrating the overall geometry and compact structure of the proposed design. The proposed antenna was designed and simulated using Computer Simulation Technology (CST) Studio Suite, which employs the Finite Integration Technique (FIT) for full-wave electromagnetic analysis. Table 1 summarizes corresponding design parameters. A two-stage CMA-based antenna optimization procedure was employed to optimize the proposed antenna.

In the first stage, the active radiator was optimized to support two dominant orthogonal characteristic modes with the required 90° phase difference for generating circular polarization. Subsequently, the feed location was optimized to efficiently excite these characteristic modes. In the second stage, four parasitic patches were symmetrically placed around the active radiator, and their dimensions and spacing were optimized to achieve strong electromagnetic coupling and wideband circular polarization. Finally, the entire antenna structure was re-

TABLE 1. Design parameters of the proposed antenna.

Parameters	Values (mm)	Parameters	Values (mm)
R_1	6	l_1	2.97
R_2	8.94	l_2	5.19
R_3	4.85	l_3	4.61
L	50	w_1	1.00
h	2.4	x_0	2.25
y_0	2.25	—	—

optimized to maximize the excitation of all contributing characteristic modes, enhancing the impedance bandwidth, axial ratio bandwidth, and broadside gain.

The circular patch can be modeled as a circular cavity resonator that supports multiple resonant modes. The resonant frequency of the TM^z_{mn0} mode is expressed as [21–23].

$$f_{r,mn0} = \frac{c}{2\pi a\sqrt{\varepsilon_r}}\, x'_{mn} \tag{1}$$

where a is the radius of the circular patch (as shown in Fig. 1); c is the speed of light in free space; and x'_{mn} represents the nth root of the derivative of the Bessel function that determines the resonant frequency order. For the first-order mode, $x'_{mn} = 1.8412$. This fundamental mode is the dominant radiating mode and initiates the circular polarization mechanism when coupled with an orthogonal mode through diagonal feeding and slot perturbation. It serves as the radiation's primary source and forms the basis for circular polarization by exciting two orthogonal degenerate modes with a quadrature (90°) phase difference using the diagonal feed and slot-perturbation technique.

2.2. Designing Active Patch Antenna Element

In Fig. 2(a), Antenna-1 consists of a simple circular patch excited by a diagonal coaxial feed positioned at (x_0, y_0) to excite two orthogonal characteristic modes. This configuration primarily supports a single dominant mode with linear polarization due to the absence of any symmetry perturbation on the patch.

In Fig. 2(b), Antenna-2 incorporates a pair of slots with dimensions l_1 and w_1, symmetrically etched on opposite sides of the circular patch. Introducing these slots perturbs the surface-current distribution and facilitates the generation of two orthogonal degenerate modes with equal amplitude and a 90° phase difference, thereby satisfying the circular polarization (CP) condition. This modification effectively transforms Antenna-1's linear polarization into circular polarization while simultaneously improving impedance matching.

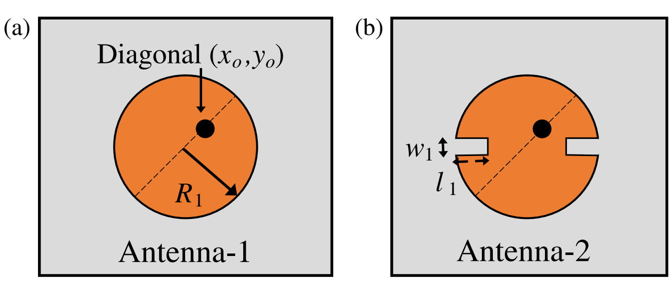

FIGURE 2. Illustrate the active antenna: (a) Antenna-1 and (b) Antenna-2.

Characteristic Mode Analysis (CMA) provides a rigorous electromagnetic framework for investigating the inherent resonant behavior of conducting structures independent of excitation. It is based on the eigenvalue problem derived from the Method of Moments (MoM) [16, 24, 25]. The Modal Significance (MS) and Characteristic Angle (CA), which are used to evaluate the radiation performance of each mode, are defined as [16]:

$$MS = \left|\frac{1}{1 + j\lambda_n}\right| \tag{2}$$

$$CA = 180^\circ - \tan^{-1}(\lambda_n) \tag{3}$$

A mode exhibits significant radiation when $MS \approx 1$ or when its Characteristic Angle (CA) approaches 180°, indicating resonance. The characteristic angle generally varies between 90° and 270° and represents the phase difference between the characteristic current and the characteristic field E^i [16, 26–28].

Fig. 3 illustrates CMA results via surface current distributions of Antenna-1 and Antenna-2. For Antenna-1, Mode 1 and Mode 2 are orthogonal characteristic modes oriented along the x- and y-directions, respectively. However, these modes are not in phase quadrature, resulting in linear polarization. In contrast, the slot perturbations introduced in Antenna-2 enable coupling between Mode 1 and Mode 2, establishing a 90° phase difference between them. This coupling facilitates orthogonal mode excitation and produces stable circular polarization. The enhanced polarization purity and radiation efficiency are further confirmed by the increased surface current intensity and its more uniform distribution across the patch.

Figure 4 presents the Characteristic Mode Analysis (CMA) results of active antennas, namely Antenna-1 and Antenna-2, in terms of Modal Significance (MS). Fig. 4(a) shows the MS response of Antenna-1, where Mode 1 and Mode 2 are the dominant modes around 6 GHz. However, these modes do not exhibit the required degeneracy and phase-quadrature condition for circular polarization, resulting in linearly polarized radiation. Modes 3 and 4 exhibit relatively low modal significance and therefore contribute minimally to the overall radiation performance.

Figure 4(b) illustrates the MS response of Antenna-2 after introducing slot perturbations. Modes 1 and 2 exhibit closely spaced resonances with modal significance values approaching unity over the frequency range of approximately 5.86–6.20 GHz. This behavior indicates that the two modes become nearly degenerate and resonate simultaneously, generating orthogonal field components essential for achieving circular polarization (CP). Furthermore, the slot loading enhances coupling between orthogonal modes, thereby supporting a wider CP operating bandwidth. As a result, Antenna-2 exhibits improved circular polarization performance compared with Antenna-1.

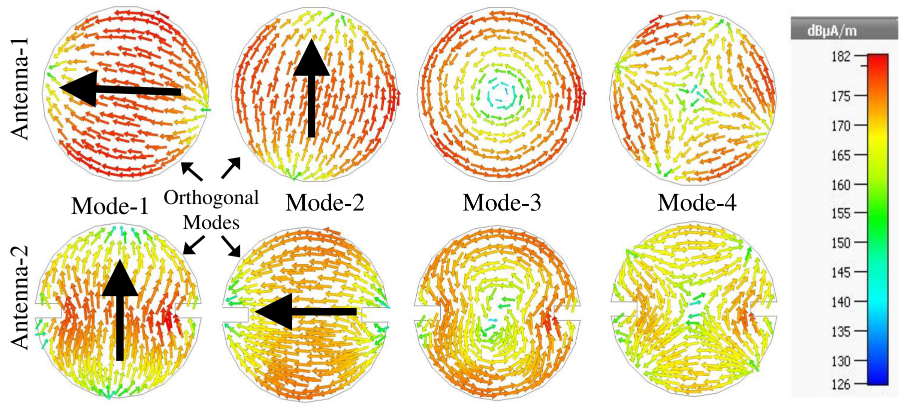

FIGURE 3. The surface current distribution of Antenna-1 and Antenna-2 by CMA.

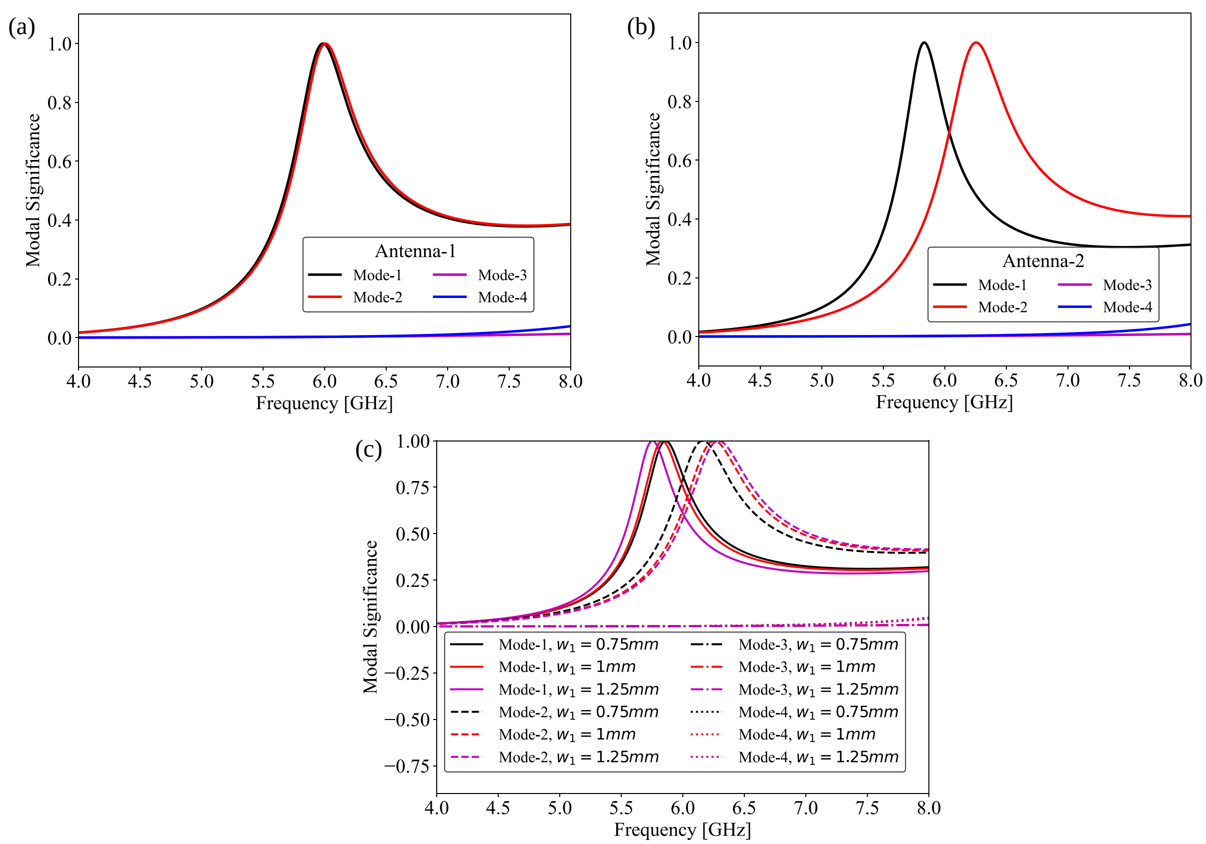

FIGURE 4. CMA analysis of the antennas: (a) MS plot of Antenna-1, (b) MS plot of Antenna-2, and (c) MS plot of Antenna-2 for different slot widths (w_1) of Antenna-2.

Tuning the modal significance of Antenna-2 depends on the slot width (w_1), as shown in Fig. 4(c). Increasing w_1 from 0.75 mm to 1.25 mm results in a slight shift of the dominant Mode-1 and Mode-2 toward lower frequencies while maintaining a modal significance (MS) value close to unity, which is favorable for strong mode excitation. In contrast, only a minor shift is observed in Mode-3, whereas Mode-4 remains nearly unchanged. Therefore, the slot width (w_1) provides an effective means of tuning the resonant frequencies of the dominant characteristic modes, facilitating wideband circular polarization.

Figure 5 illustrates the variation of the Characteristic Angle (CA) between orthogonal modes of Antenna-1 and Antenna-2. In Antenna-1, the CA separation between the two dominant modes remains significantly different from 90°, indicating that the required phase relationship for circular polarization is not achieved. Consequently, the antenna exhibits linear polarization characteristics. In contrast, for Antenna-2, the CA difference approaches 90° around 6 GHz. This satisfies the fundamental condition for circular polarization, in which two orthogonal modes must have nearly equal amplitudes and a quadrature (90°) phase difference. The results clearly demonstrate that the introduced slot perturbation facilitates proper coupling between the orthogonal modes and establishes the desired phase relationship, thereby enabling and sustaining circular polarization.

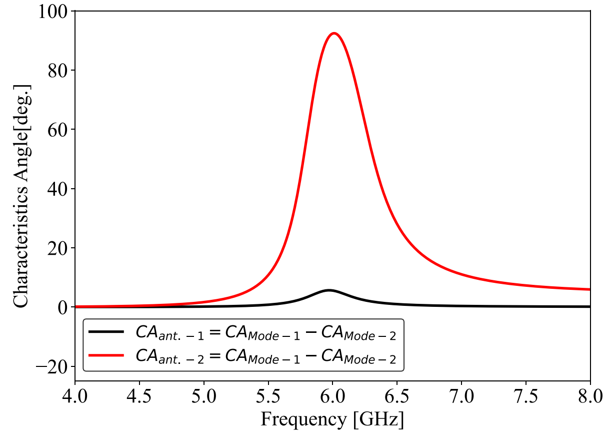

FIGURE 5. Illustrates the characteristic angle difference between the orthogonal modes for Antenna-1 and Antenna-2.

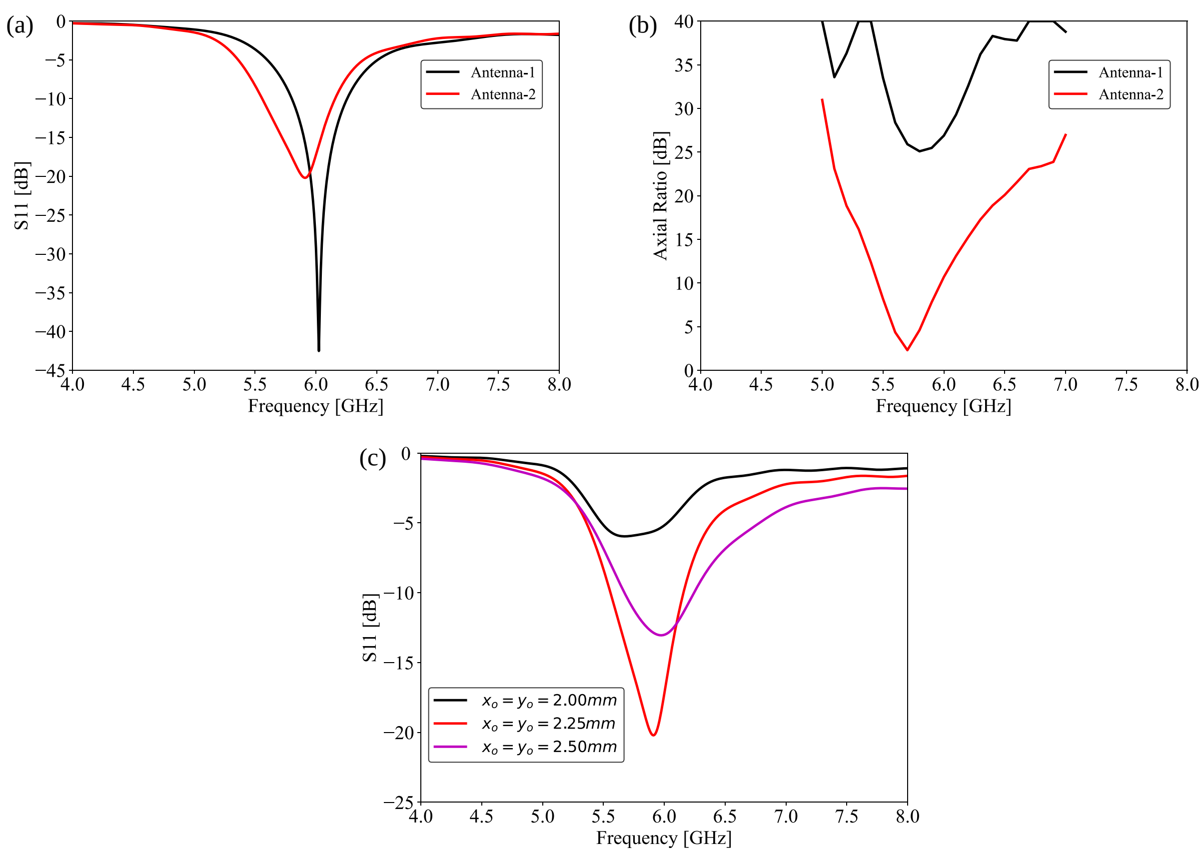

FIGURE 6. Full-wave EM analysis of the antennas with feed: (a) reflection coefficient (S_{11}), (b) axial ratio (AR), and (c) S_{11} plot with different feed locations.

Fig. 6(a) compares reflection coefficient (S_{11}) responses of the two antennas. Both antennas resonate within the frequency range of approximately 5.8–6.0 GHz. However, Antenna-2 provides a wider impedance bandwidth than Antenna-1, although its minimum S_{11} level is relatively higher. This indicates that Antenna-2 offers broader impedance matching rather than deeper impedance matching. This improvement is attributed to slot perturbation and optimized feed position, which effectively reduce input impedance mismatch.

Figure 6(b) presents the antennas' axial ratio (AR) characteristics. The results indicate that Antenna-1 remains linearly polarized, with an AR exceeding 10 dB throughout the operating band. In contrast, Antenna-2 achieves an AR below 3 dB over the frequency range of 5.7–5.8 GHz, confirming the generation of circular polarization. These findings are consistent with the CMA predictions and validate the effectiveness of the slot perturbation in establishing the required orthogonal mode excitation and phase relationship for circular polarization.

Figure 6(c) illustrates the effect of the feed position ($x_0 = y_0$) on the reflection coefficient (S_{11}) of the proposed antenna. Feed location strongly influences the input impedance and impedance matching. Among the investigated positions,

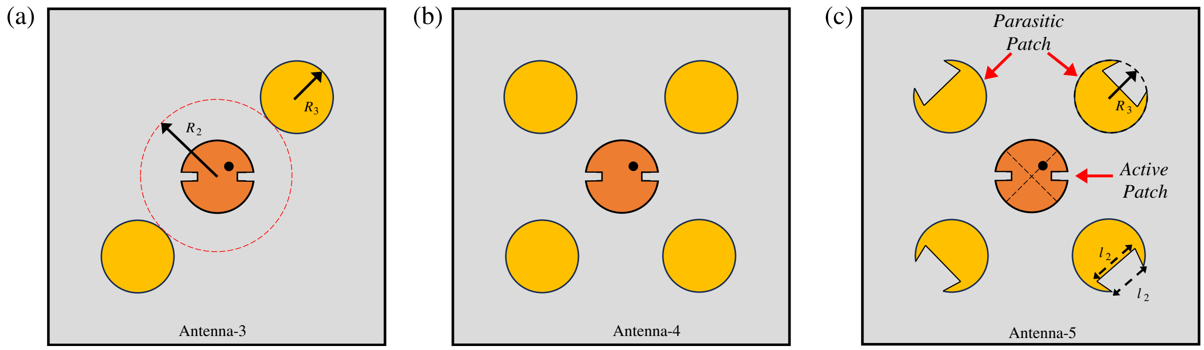

FIGURE 7. Illustrates the parasitic patch loading with the active patch: (a) $N = 2$, (b) $N = 4$, and (c) $N = 4$ (modified parasitic patch).

$x_0 = y_0 = 2.25$ mm provides the best impedance matching, exhibiting the deepest resonance ($S_{11} \approx -20$ dB) at approximately 5.9 GHz. In comparison, feed positions of 2.0 mm and 2.5 mm result in inferior impedance matching. Therefore, the optimized feed position of $x_0 = y_0 = 2.25$ mm is selected for the proposed antenna design.

2.3. Loading Parasitic Element with Active Patch Antenna

Fig. 7 illustrates evolution of the proposed antenna geometry through progressive parasitic patch loading. The active circular patch is successively loaded with parasitic elements to enhance the antenna gain and bandwidth. Fig. 7(a) shows Antenna-3, which consists of an active circular patch surrounded by two parasitic patches ($N = 2$) symmetrically positioned along the diagonal axis. This partial-coupling configuration provides only limited improvement in radiation performance due to the relatively weak modal interaction between the active and parasitic elements.

Figure 7(b) presents Antenna-4, where four parasitic patches ($N = 4$) are arranged orthogonally around the active patch. The increased number of parasitic elements enhances mutual coupling and improves aperture efficiency. This configuration promotes stronger excitation of orthogonal modes, resulting in moderate improvements in both impedance bandwidth and gain.

Figure 8 illustrates surface-current distributions and corresponding far-field radiation patterns of Antenna-3, Antenna-4, and Antenna-5. The results demonstrate that parasitic loading has a significant influence on the antenna's modal behavior and radiation characteristics. In Fig. 8(a), corresponding to Antenna-3, surface-current distributions indicate that Mode-1 and Mode-2 are primarily confined to the active patch, suggesting weak coupling between the active element and parasitic patches. The dominant modes are not sufficiently degenerate, leading to limited bandwidth and relatively low gain.

In Fig. 8(b), Antenna-4, surface currents are more uniformly distributed across both active and parasitic patches, confirming stronger electromagnetic coupling and improved orthogonality between dominant modes. The current distributions of Mode-1 and Mode-2 are nearly orthogonal, which facilitates the generation of circular polarization. The corresponding radiation patterns exhibit enhanced broadside directivity compared with those of Antenna-3.

Figure 8(c) shows the performance of Antenna-5, where the modified parasitic patch geometry further strengthens the field interaction via capacitive coupling and promotes a more uniform current distribution across all radiating elements. Mode-1 and Mode-2 become nearly orthogonal with comparable amplitudes, while Mode-3 and Mode-4 contribute to bandwidth enhancement. The associated radiation patterns exhibit stronger broadside radiation and higher gain, confirming that the modified parasitic geometry effectively improves aperture efficiency, mode coupling, and overall antenna performance.

Fig. 9 presents Characteristic Mode Analysis (CMA) results in terms of Modal Significance (MS) for Antenna-3, Antenna-4, and Antenna-5 to illustrate the effect of parasitic patch loading on mode excitation and bandwidth enhancement. Fig. 9(a) shows the MS response of Antenna-3, where two dominant modes (Mode-1 and Mode-2) are observed within the frequency range of approximately 5.8–6.2 GHz. However, the modal peaks are not well aligned, and their MS values are unequal, indicating weak coupling and insufficient modal degeneracy. As a result, the antenna has limited capability for circular polarization.

Figure 9(b) illustrates the modal behavior of Antenna-4 after adding four parasitic patches. Mode-1 and Mode-2 move closer together and their MS values approach unity. This behavior indicates enhanced electromagnetic coupling and improved degeneracy between dominant modes. Consequently, the antenna's radiation performance and impedance bandwidth are improved.

Figure 9(c) presents the MS characteristics of Antenna-5, where parasitic patches are modified by introducing slots. In this configuration, the two dominant modes overlap over a wider frequency range, allowing both modes to contribute more equally to radiation. This results in an enhanced circular polarization bandwidth and improved modal balance. In addition, the higher-order modes (Mode-3 and Mode-4) become resonant and participate in radiation, contributing to bandwidth enhancement via introducing additional coupling paths.

Figure 10(a) shows the variation of the Characteristic Angle (CA) for the two dominant orthogonal modes of Antenna-2, Antenna-3, Antenna-4, and Antenna-5. For Antenna-2 and Antenna-3, the CA difference remains significantly below 90°,

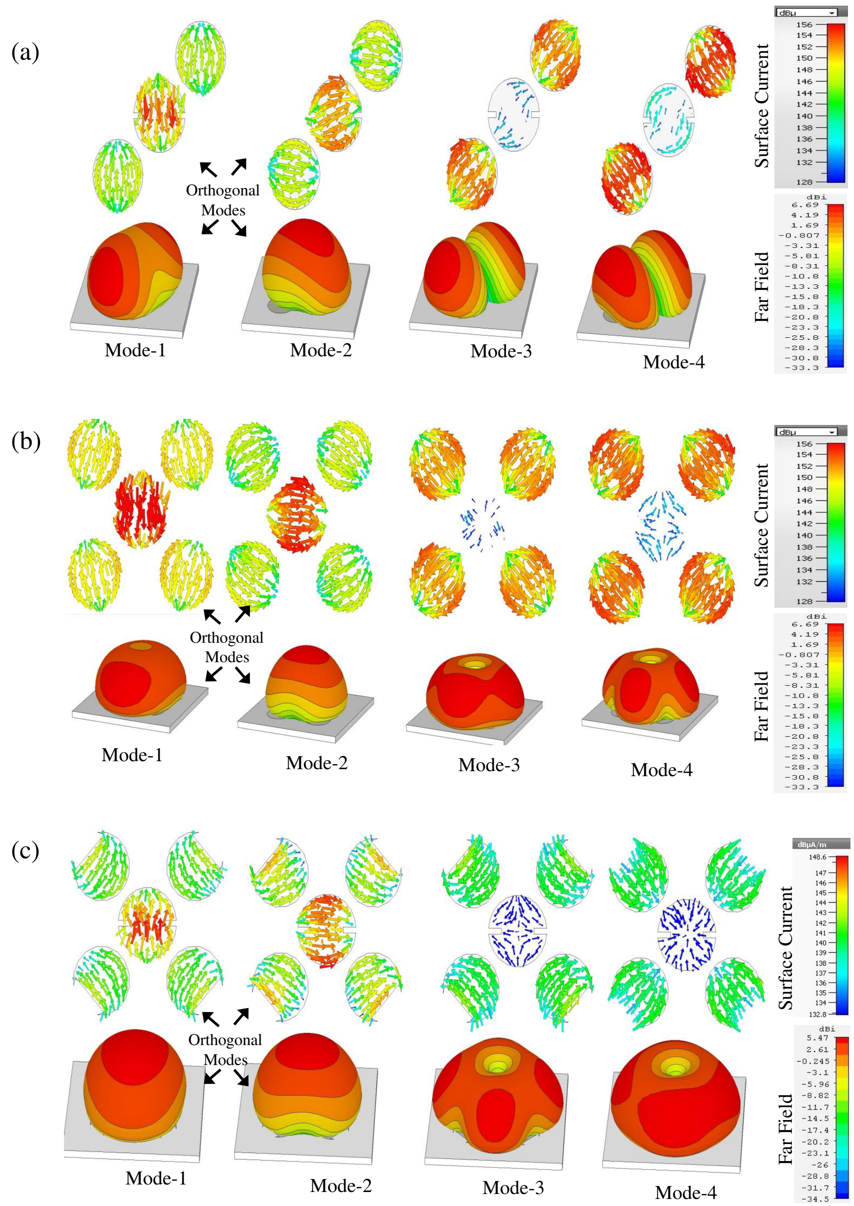

FIGURE 8. Surface current distributions and corresponding radiation patterns for different modes of the proposed antenna configurations: (a) Antenna-3, (b) Antenna-4, and (c) Antenna-5.

indicating that the excited modes are not in phase quadrature and therefore produce linear polarization. With the introduction of four parasitic patches in Antenna-4, the CA difference approaches 90° near 6.0 GHz, satisfying the condition required for circular polarization (CP). In Antenna-5, the modified parasitic geometry further stabilizes the phase relationship between the dominant modes and maintains a phase difference close to 90° over a broader frequency range. This behavior confirms that Antenna-5 provides stronger orthogonal mode excitation and achieves a wider axial ratio bandwidth (ARBW) than preceding antenna configurations.

Fig. 10(b) shows results of the eigenvalue variation for the first four characteristic modes of Antenna-5. The eigenvalues of Modes 1–4 converge to zero around 6.2 GHz, which corresponds to a modal resonance. Dominant resonant modes 1 and 2 mainly contribute to modal radiation and are responsible for circular polarization, while Modes 3 and 4 contribute comparatively small radiation.

Fig. 11(a) shows simulated reflection coefficients (S_{11}) for different values of the parasitic patch radius (R_3). Varying R_3 modifies the electromagnetic coupling between the active radiator and the parasitic patches, thereby influencing the resonant frequency and impedance matching. Among the investigated values, $R_3 = 4.85$ mm provides the best impedance matching, exhibiting the deepest resonance at approximately 6 GHz. Therefore, $R_3 = 4.85$ mm is selected as the optimum parasitic patch radius.

Figure 11(b) illustrates the variation of the reflection coefficient (S_{11}) with the spacing (R_2) between active and parasitic patches. Adjusting R_2 controls the strength of the electromagnetic coupling, which in turn affects the resonant frequencies and impedance matching. The optimum spacing is

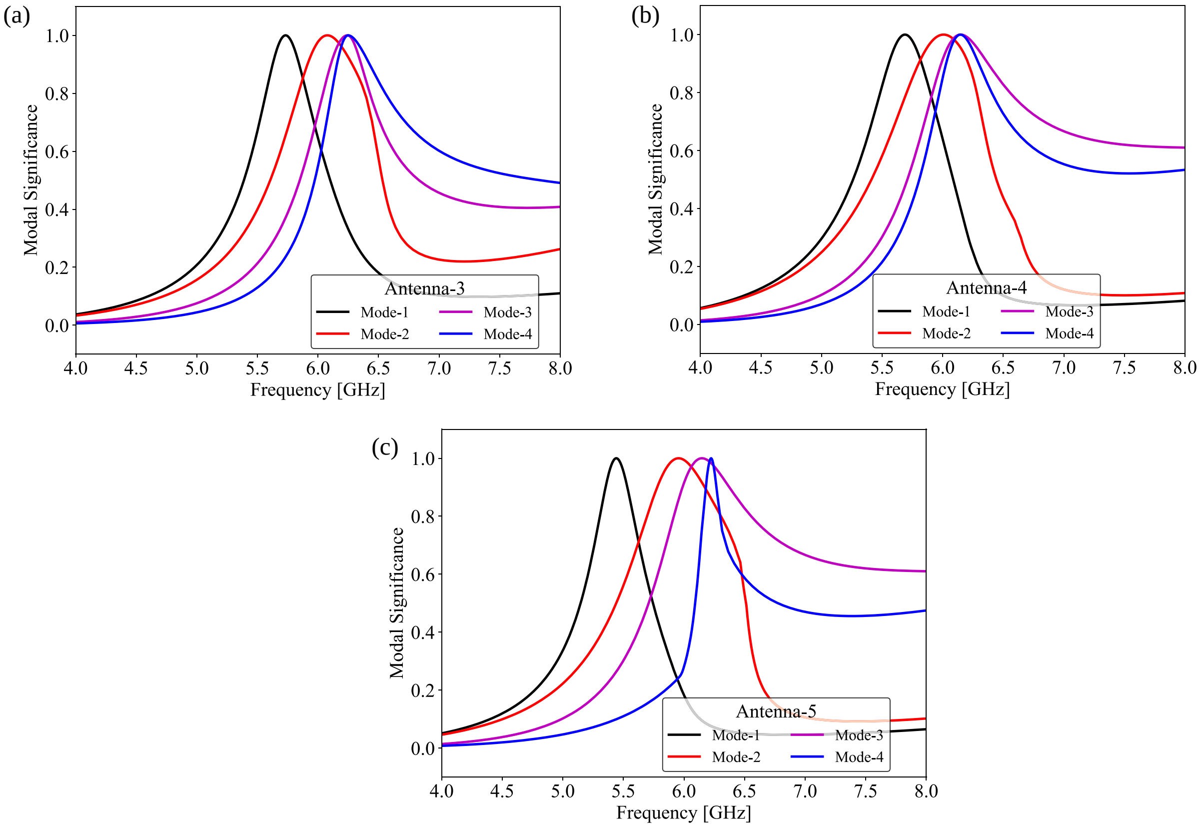

FIGURE 9. Illustrates the CMA analysis of Antennas: (a) MS plot of Antenna-3, (b) MS plot of Antenna-4, and (c) Antenna-5.

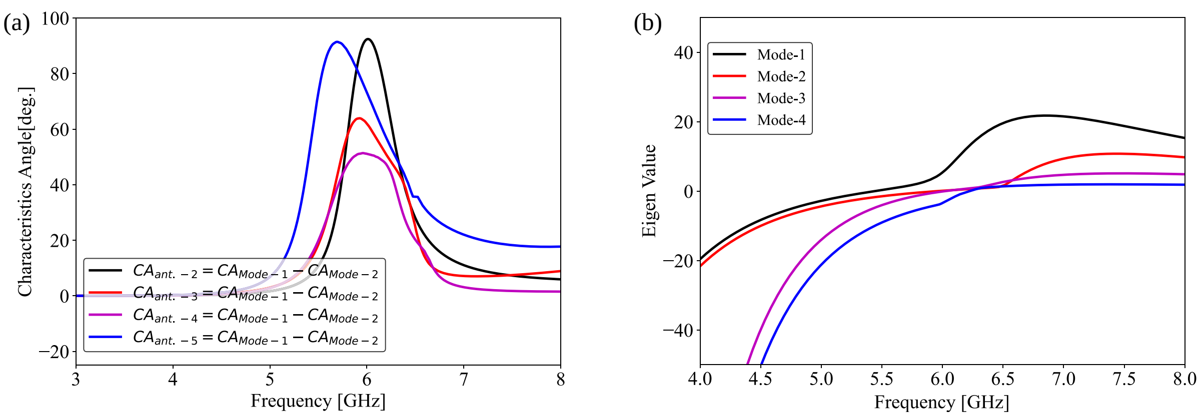

FIGURE 10. Characteristic Mode Analysis (CMA) results: (a) Characteristic angle difference between the orthogonal modes of Antennas 2, 3, 4, and 5, and (b) eigenvalue plot of Antenna 5.

$R_2 = 8.94$ mm, providing the best impedance matching and the desired operating bandwidth. Smaller or larger spacing results in over-coupling or under-coupling, respectively, leading to degraded antenna performance.

Fig. 12 presents complete full-wave electromagnetic (EM) simulation results of the proposed antenna configurations and compares reflection coefficients (S_{11}) and axial ratios (ARs) of Antenna-2, Antenna-3, Antenna-4, and Antenna-5.

Figure 12(a) shows antennas' S_{11} responses. All antenna configurations resonate within the frequency range of approximately 5.4–6.4 GHz, with impedance matching progressively improving as additional parasitic patches are incorporated. Antenna-2 exhibits a single resonance around 5.9 GHz with a relatively narrow impedance bandwidth. In contrast, Antenna-3 and Antenna-4 provide broader impedance bandwidths due to enhanced electromagnetic coupling between active and parasitic patches. Antenna-5, which incorporates modified parasitic elements, has the best impedance matching performance, achieving a deep reflection coefficient of approximately -40 dB and the widest -10 dB impedance bandwidth among all antenna configurations.

This improvement confirms that optimization of the parasitic patch geometry significantly enhances electromagnetic coupling and overall impedance performance. Fig. 12(b) compares

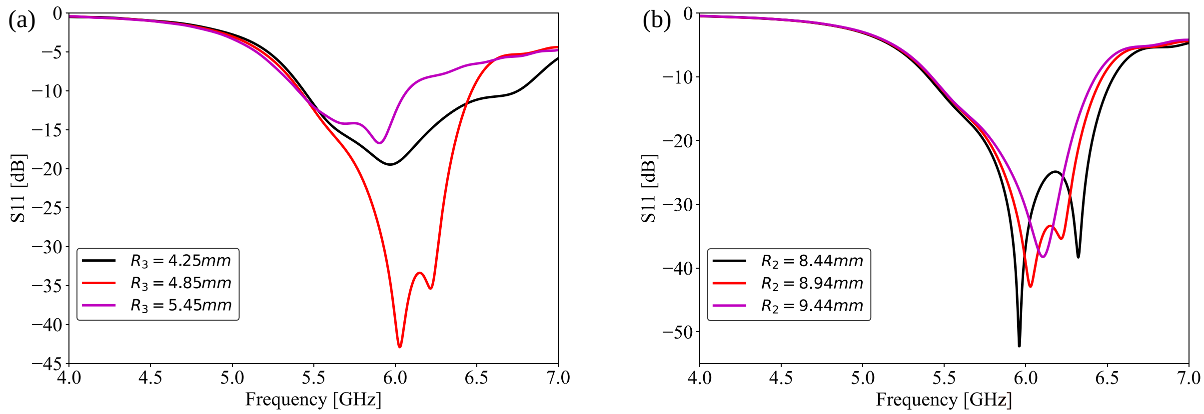

FIGURE 11. Parametric study with (a) R_3 parameter and (b) R_2 parameter.

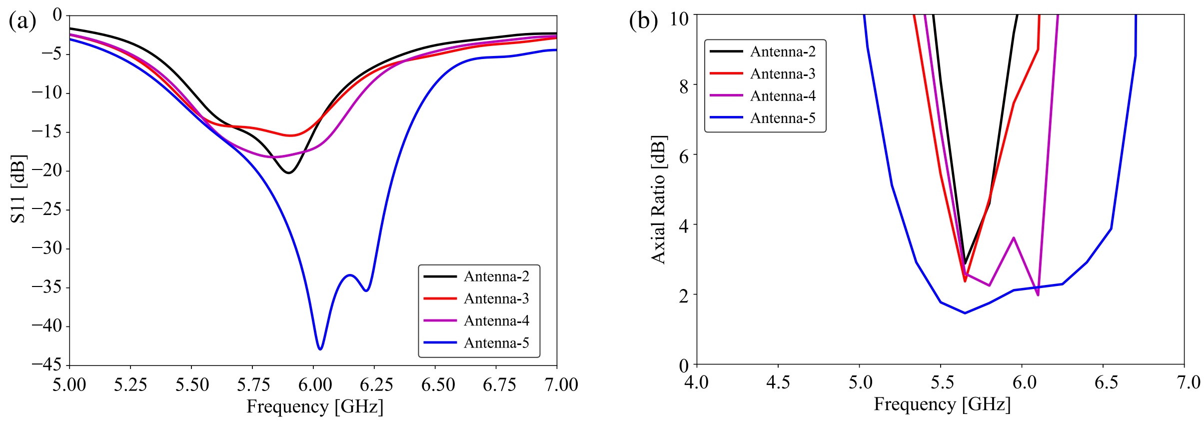

FIGURE 12. Shows the full-wave EM analysis of the antennas with feed: (a) S_{11} and (b) axial ratio.

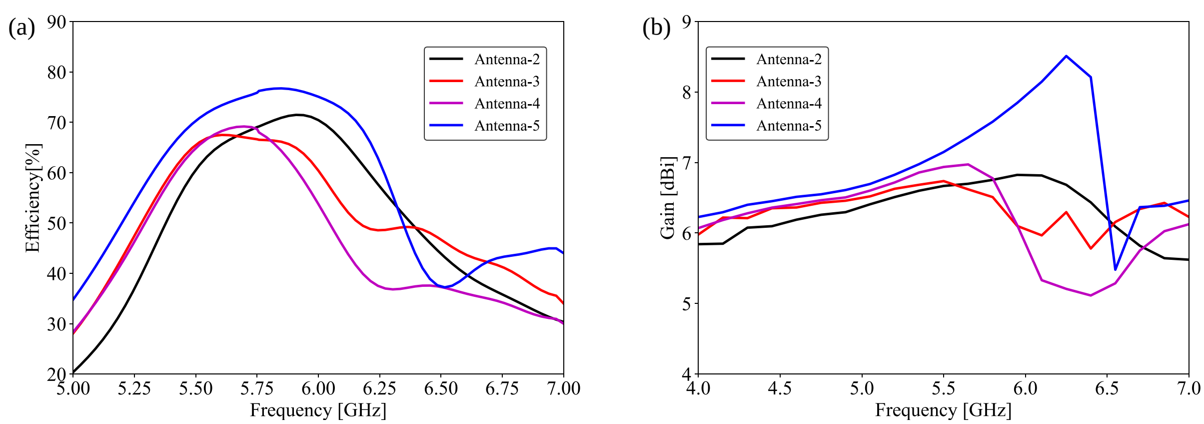

FIGURE 13. Shows the full-wave EM analysis of the antennas with feed: (a) Efficiency and (b) gain.

the axial ratio (AR) characteristics of the antennas and illustrates the evolution from linear to circular polarization across the design stages. Antenna-2 and Antenna-3 exhibit AR values greater than 6 dB in most of the operating band, indicating predominantly linear polarization. Antenna-4 begins to exhibit circular polarization around 5.8 GHz, where the AR falls below 3 dB within a relatively narrow frequency range. In contrast, Antenna-5 achieves a substantially wider 3-dB axial ratio bandwidth (ARBW) extending from 5.35 GHz to 6.40 GHz, confirming stable circular polarization performance resulting from the balanced excitation of orthogonal modes.

Fig. 13 presents the radiation performance of the proposed antenna configurations, which compares the total efficiency and gain characteristics of different antenna designs. Fig. 13(a) shows that the total efficiency increases progressively with the addition of parasitic patches. Antenna-2 has an average total efficiency of about 55%, while Antenna-3 and Antenna-4 achieve efficiencies in 65%–70%. Antenna-5 demonstrates the highest performance, with a peak total efficiency of approximately 80% at 5.8 GHz. This improvement indicates more effective radiation of the input power and reduced surface-wave losses, resulting from enhanced impedance matching and stronger modal coupling.

The gain characteristics shown in Fig. 13(b) follow a similar trend. Antenna-2 and Antenna-3 provide moderate gains in 5–6.5 dBi, while Antenna-4 has a slight improvement. Antenna-5 achieves the highest broadside gain, reaching approximately 8.5 dBi at 5.9 GHz. This gain enhancement is attributed to improved aperture efficiency and constructive radiation resulting from the optimized coupling between the active and parasitic elements.

Figure 14 illustrates surface-current distributions of the proposed antenna at different phase angles of $0°$, $90°$, $135°$, and $180°$. Surface-current vectors rotate counterclockwise $(-z)$ with increasing phase, indicating the generation of Right-Hand Circular Polarization (RHCP). The two orthogonal modes maintain nearly equal amplitudes with a $90°$ phase difference, satisfying the fundamental condition for circular polarization. These results confirm that the proposed antenna radiates a stable RHCP wave and maintains consistent current rotation throughout the operating frequency band.

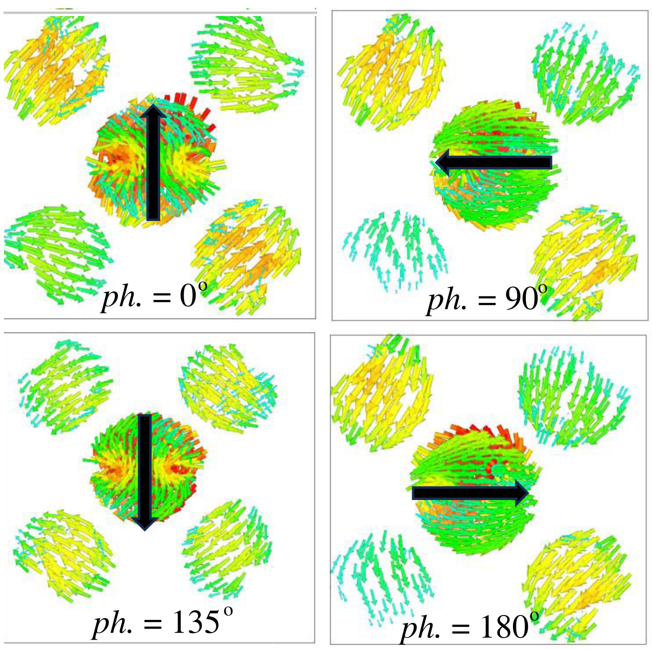

FIGURE 14. Illustrates the surface current distribution of the proposed antenna at different phase angles.

3. EQUIVALENT CIRCUIT MODELING OF PROPOSED ANTENNA

Figure 15 presents the equivalent circuit modeling (ECM) of the proposed parasitic patch antenna and its comparison with the electromagnetic (EM) simulation response. The proposed antenna consists of a centrally placed active circular patch surrounded by four parasitic circular patches printed on an FR4 substrate. The active patch is excited using a coaxial feed at the optimized position (x_o, y_o), while surrounding parasitic patches are electromagnetically coupled to the active radiator to improve bandwidth and resonance characteristics.

To analyze the antenna's electrical behavior, we develop an equivalent circuit model using lumped RLC elements, as shown in Fig. 15(a). The active radiating patch is represented by components L_a, C_a, and R_a, where L_a denotes the inductive effect from current flow; C_a represents the capacitance generated between conducting regions; and R_a models radiation and conduction losses. Similarly, each parasitic patch is modeled using L_p, C_p, and R_p, which characterize the resonant behavior of parasitic elements. The electromagnetic coupling between the active patch and parasitic patches is represented by coupling capacitance C_c. The feeding mechanism is modeled using feed inductance L_f and feed resistance R_f connected to the input port with characteristic impedance Z_o. Electrical parameters of the equivalent circuit are extracted via an iterative comparison between S_{11} characteristics obtained from the EM simulation and ECM response. Optimized extracted values are presented in Table 2.

TABLE 2. ECM parameters of proposed antenna.

Parameters	Values	Parameters	Values
L_f	0.11 nH	L_p	0.432 nH
R_f	9.4 Ω	C_p	1.49 pF
L_a	0.39 nH	R_p	315.97 Ω
C_a	1.56 pF	C_c	0.049 pF
R_a	46.65 Ω	—	—

Figure 15(b) compares reflection coefficient (S_{11}) characteristics obtained from the full-wave EM simulation and the proposed ECM analysis. The solid curve represents the EM-simulated response, whereas the dashed curve corresponds to the ECM response. The two results show close agreement in the operating frequency range, confirming the validity of the developed equivalent circuit model. The close correlation between the EM and ECM responses demonstrates that the proposed equivalent circuit accurately models the antenna's resonant behavior, coupling mechanism, and impedance characteristics while simplifying analysis and design.

4. PROPOSED ANTENNA HARDWARE FABRICATION AND MEASUREMENT

Figure 16 depicts the fabricated prototype of the proposed antenna and the experimental setup used for validation. Fig. 16(a) shows the fabricated hardware of the proposed antenna. Fig. 16(b) illustrates the measurement configuration using a Vector Network Analyzer (VNA) to measure the reflection coefficient (S_{11}) of the fabricated antenna. The VNA is connected to the antenna under test (AUT) through an SMA connector, and the measured S_{11} results are compared with the simulated values obtained from full-wave electromagnetic (EM) analysis. Fig. 16(c) shows the anechoic chamber setup used for radiation pattern and axial ratio (AR) measurements. The antenna is mounted on a non-reflective stand in the far-

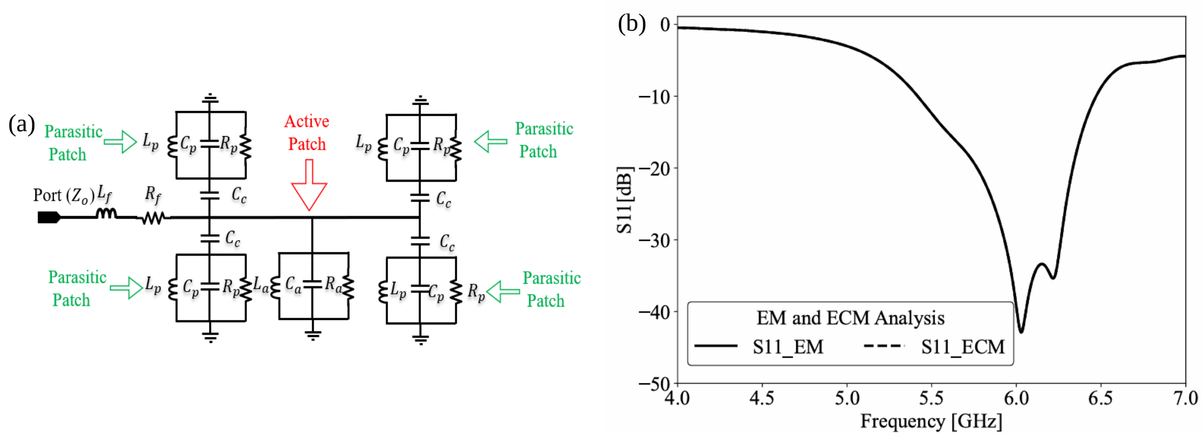

FIGURE 15. Illustrates Equivalent Circuit Modeling of the proposed antenna, (a) ECM model and (b) S_{11} comparison between ECM and EM.

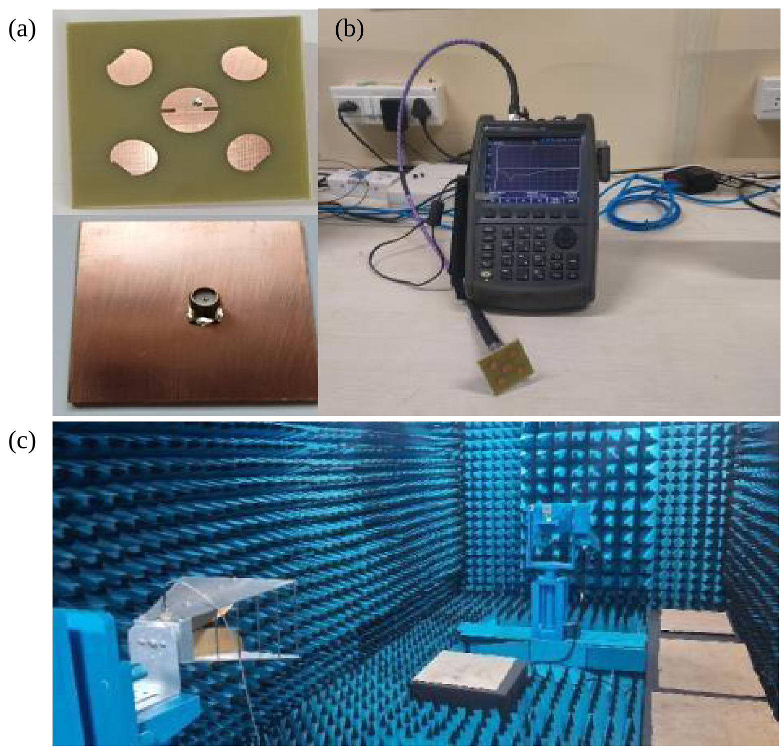

FIGURE 16. Shows the photographs of the fabricated antenna prototype and the measurement setup: (a) the fabricated hardware, (b) the Vector Network Analyzer (VNA), and (c) the anechoic chamber.

field region of a standard horn antenna acting as the transmitter. This arrangement enables accurate measurements of broadside radiation characteristics, gain, and polarization performance while minimizing external reflections and interference.

Figure 17 presents the comparison between full-wave EM simulated and measured results of the proposed circularly polarized antenna. Fig. 17(a) compares reflection coefficient (S_{11}) characteristics and shows excellent agreement between simulated and measured results. The measured -10 dB impedance bandwidth is 18.12% (5.42–6.50 GHz), which closely matches the simulated value. Minor discrepancies can be attributed to fabrication tolerances, SMA connector losses, and manual soldering effects. Both curves exhibit a strong resonance near 5.9 GHz, validating that the designed feed structure and parasitic coupling provide effective impedance matching.

Figure 17(b) compares axial ratio (AR) characteristics and further confirms the accuracy of the simulation model. The measured 3 dB AR bandwidth is 17.87% (5.35–6.40 GHz), which agrees well with the simulated response. The slight upward shift observed in the measured curve may be attributed to substrate inhomogeneity and environmental variations during anechoic chamber testing. The close agreement between simulated and measured AR results verifies that the proposed antenna successfully achieves broadband circular polarization.

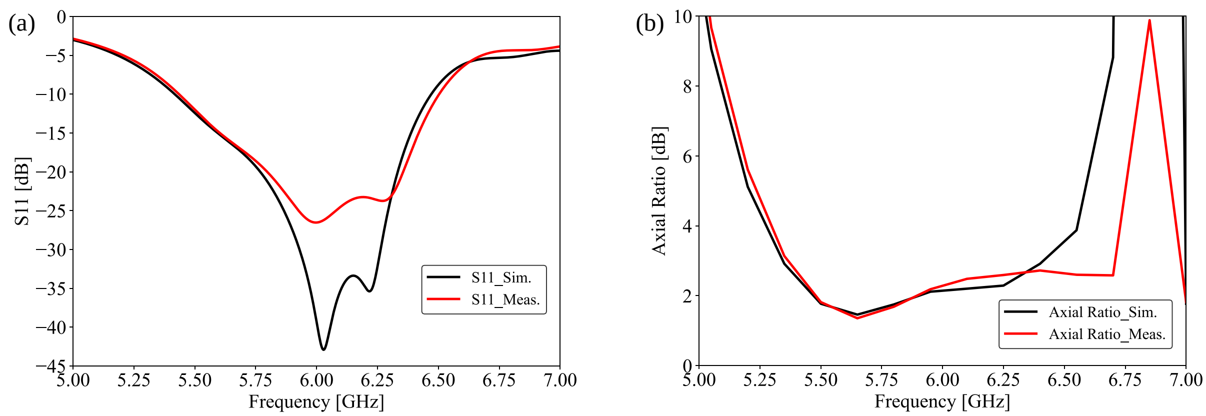

FIGURE 17. Shows the comparison between simulated (EM) and measured results: (a) S_{11} and (b) axial ratio.

TABLE 3. Related work comparisons.

Ref.	Band (GHz)	IM BW (%)	AR BW (%)	Size (λ_0)	Gain (dBi)	Printed Layers	Pattern
This work	C-band	18.12	17.87	$0.91 \times 0.91 \times 0.04$	7.1	1	Broadside
[29]	S-band	49.8	24	$0.97 \times 0.97 \times 0.11$	8.0	Air gap	Broadside
[24]	1.4–2.3	40.3	31.6	$0.8 \times 0.8 \times 0.167$	8.0	3 + Air gap	Broadside
[13]	C-band	46	28.9	$0.98 \times 0.912 \times 0.065$	6.8	2	Broadside
[2]	C-band	14.7	14.7	$1.18 \times 1.18 \times 0.05$	10.8	1	Broadside
[5]	C-band	23.1	9.6	$1.42 \times 1.42 \times 0.5$	7.45	1	Conical Beam
[6]	S-band	23.25	5.1	$0.43 \times 0.43 \times 0.024$	4.54	1	Broadside
[30]	C-band	35.1	17.5	$0.92 \times 0.92 \times 0.6$	8.5	2	Monopole
[31]	C-band	3.97	2.93	$0.53 \times 0.53 \times 0.18$	2.1	Air gap	Omni-directional
[14]	C-band	39.5	33.1	$0.9 \times 0.9 \times 0.05$	9.4	2	Broadside
[15]	C-band	81.25	30.7	$0.52 \times 0.52 \times 0.2$	3.8	1	Monopole
[16]	S-band	18	14.3	$1.04 \times 1.04 \times 0.027$	8.9	1	Broadside
[18]	C-band	33	20	$1.76 \times 1.76 \times 0.07$	8.5	2	Broadside
[19]	C-band	48.6	20.4	$0.6 \times 0.58 \times 0.7$	6.52	2	Broadside
[20]	C-band	16	14.4	$0.46 \times 0.46 \times 0.05$	7.0	2	Broadside
[32]	S-band	5.6	2.2	$0.49 \times 0.49 \times 0.014$	4.65	1	Broadside
[8]	C-band	9.5	–	$1.41 \times 1.06 \times 0.06$	8.8	2	Broadside
[9]	26.6–31.5	31.7	16.9	$0.52 \times 0.52 \times 0.17$	5.1	3	Broadside
[10]	8.76–10.74	–	20.3	$0.79 \times 0.79 \times 0.023$	8.1	1	Broadside
[11]	1.17–1.59	3.6	3.8	$0.35 \times 0.35 \times 0.02$	6.5	3 (Air gap)	Broadside
[12]	4.38–11.78	–	10.18	$0.42 \times 0.42 \times 0.02$	4.97	1	Bidirectional
[33]	2.4–7.4	102	37.8	$0.25 \times 0.31 \times 0.01$	2.4	1	Bidirectional
[34]	2.42–8.7	–	46.6	$0.25 \times 0.31 \times 0.01$	1.2	1	Bidirectional
[35]	3.96–6.55	49	17.69	$0.57 \times 0.53 \times 0.02$	3.02	1	Bidirectional

Figure 18 compares full-wave electromagnetic (EM) simulated and measured results of the proposed circularly polarized antenna. Fig. 17(a) shows that measured reflection coefficient (S_{11}) characteristics are in close agreement with simulated results. The measured -10 dB impedance bandwidth is 18.12% (5.42–6.50 GHz), which closely matches the simulated bandwidth. Minor deviations between simulated and measured responses can be attributed to fabrication tolerances, SMA connector losses, and manual soldering effects.

Both curves exhibit a strong resonance near 5.9 GHz, confirming that the designed feed structure and parasitic coupling provide effective impedance matching. Fig. 17(b) presents the comparison of the axial ratio (AR) characteristics, further validating the accuracy of the simulation model. The measured 3 dB AR bandwidth is 17.87% (5.35–6.40 GHz), which agrees well with the simulated response. The slight upward shift observed in the measured curve may be attributed to substrate inhomogeneity and environmental variations during anechoic

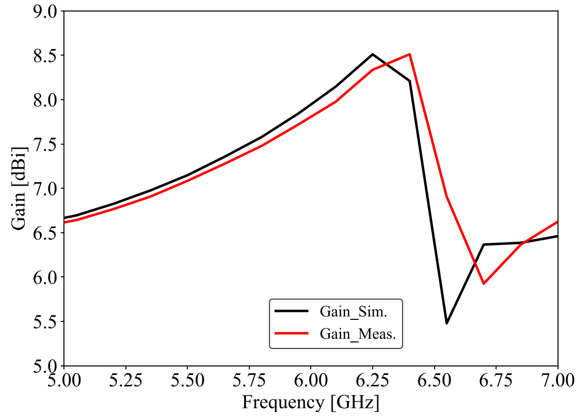

FIGURE 18. Shows the Gain comparison between simulated and measured results.

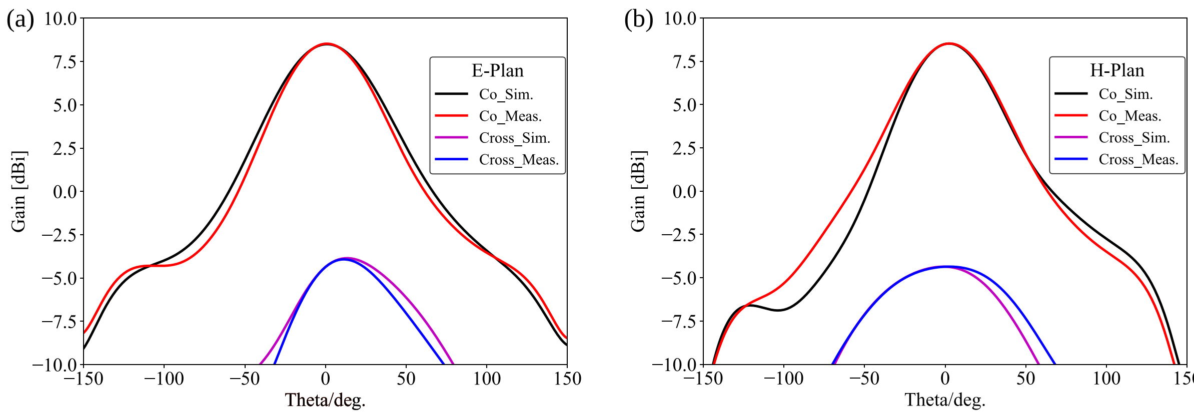

FIGURE 19. Shows simulated and measured radiation patterns: (a) E-plane and (b) H-plane.

chamber testing. The close agreement between EM-simulated and measured AR results verifies that the proposed antenna successfully achieves broadband circular polarization.

Fig. 18 presents the comparison between simulated and measured gain responses of the proposed antenna in the operating frequency range. Both results exhibit a similar trend, showing a stable gain performance throughout the frequency range of 5.4–6.0 GHz. The measured broadside gain reaches approximately 8.5 dBi, which is in close agreement with the simulated peak gain. Minor discrepancies between the simulated and measured curves can be attributed to fabrication tolerances, cable losses, connector effects, and measurement system calibration uncertainties. The close agreement between simulated and measured results validates the accuracy of the design methodology and confirms the effectiveness of the parasitic loading technique in enhancing the antenna's aperture efficiency and radiation performance.

Figure 19 presents simulated and measured radiation patterns of the proposed antenna at the operating frequency for both the E-plane and H-plane cuts. Fig. 19(a) illustrates the E-plane radiation pattern, where simulated and measured co-polarization responses are in excellent agreement. Both results exhibit low cross-polarization levels and a stable broadside radiation pattern. The measured results closely follow the simulated characteristics, confirming the accuracy of the electromagnetic model and demonstrating stable circular-polarization performance in the main-beam direction.

Figure 19(b) shows the antenna's H-plane radiation pattern. A symmetric radiation beam with strong cross-polarization suppression is observed in both the simulated and measured results. The measured patterns closely match simulated trends, validating polarization behavior and confirming uniform field distribution across principal radiation planes. These results demonstrate the effectiveness of the proposed antenna in maintaining stable radiation characteristics and high polarization purity throughout the operating band. Table 3 presents the comparison between the proposed work and related references.

5. CONCLUSION

This paper has developed a CMA-based wideband circularly polarized antenna that has been analyzed and experimentally proven. We developed the design procedure methodologically from a simple circular patch to a parasitically loaded configuration optimized for broadband circular polarization and high gain. CMA identified the dominant orthogonal modes required to generate circular polarization. By combining slot perturbation with a diagonal coaxial feed, a 90-degree phase difference and equal modal amplitudes were achieved. Introducing four parasitic patches around the active element greatly enhances the efficiency of aperture, impedance bandwidth, and axial ratio bandwidth due to high-degree electromagnetic coupling between active and parasitic resonators. More optimization of the parasitic geometry resulted in better mode coupling, which produced stable broadside radiation. Measured values attained an impedance bandwidth of −10 dB of 18.12% (5.42 6.50 GHz), a 3 dB axial ratio bandwidth of 17.87% (5.35–6.40 GHz), and a broadside gain of 8.5 dBi.

REFERENCES

[1] Bag, B., R. Mondal, S. Biswas, and P. P. Sarkar, "Application-based evolution of microstrip antenna: Presenting wide-bandwidth circular polarization and multi-resonating characteristics," *Journal of Electromagnetic Waves and Applications*, Vol. 34, No. 14, 1899–1917, 2020.

[2] Hussain, N., H. H. Tran, and T. T. Le, "Single-layer wideband high-gain circularly polarized patch antenna with parasitic elements," *AEU — International Journal of Electronics and Communications*, Vol. 113, 152992, 2020.

[3] Suyan, N. K., F. L. Lohar, Y. Solunke, and C. Dhote, "Design of compact size tri-band stacked patch antenna for GPS and IRNSS applications," in *Congress on Intelligent Systems*, 501–509, Springer, Singapore, 2020.

[4] Maurya, R. K., B. K. Kanaujia, A. K. Gautam, S. Chatterji, and A. K. Singh, "Circularly polarized hexagonal ring microstrip patch antenna with asymmetrical feed and DGS," *Microwave and Optical Technology Letters*, Vol. 62, No. 4, 1702–1708, 2020.

[5] Xu, H., J. Zhou, K. Zhou, and Z. Yu, "Low-profile circularly polarised patch antenna with high gain and conical beam," *IET Microwaves, Antennas & Propagation*, Vol. 12, No. 7, 1191–1195, 2018.

[6] Shaw, M., N. Mandal, and M. Gangopadhyay, "A compact circularly polarized isosceles triangular microstrip patch antenna with parasitic elements for multiband application," *Microwave and Optical Technology Letters*, Vol. 62, No. 10, 3275–3282, 2020.

[7] Rashmi, , A. Kumar, K. Saraswat, and A. Kumar, "Wideband circularly polarized parasitic patches loaded coplanar waveguide-fed square slot antenna with grounded strips and slots for wireless communication systems," *AEU — International Journal of Electronics and Communications*, Vol. 114, 153011, 2020.

[8] Tran, H., P. Kim-Thi, N. Tran, T. Hoang-Thi-Phuong, and Y. Vu-Van, "A novel approach to design compact, wideband, and high-gain circularly polarized MIMO antenna using dual-polarized elements and hybrid couplers," *Scientific Reports*, Vol. 15, No. 1, 45100, 2025.

[9] Du, K., Z. Huang, X. Xu, J. Hao, Q. Pang, and J. Ouyang, "A wideband dual-port selectable RHCP/LHCP polarized antenna for satellite communications," *IEEE Antennas and Wireless Propagation Letters*, 1–5, 2026.

[10] Shrivastava, M. K., R. Singh, D. Samantaray, A. Khan, A. K. Gautam, and A. K. Singh, "A metamaterial loaded high gain low profile RHCP microstrip antenna for X-band applications," *IEEE Access*, Vol. 13, 33 321–33 329, 2025.

[11] Deng, Z., J. Li, H. Peng, Q. Zou, P. Xiao, and G. Li, "Compact dual-mode CP antenna with wide AR beamwidths for BDS-based vehicular applications," *IEEE Open Journal of Antennas and Propagation*, Vol. 7, No. 3, 838–848, 2026.

[12] Sridhar, P. and R. Poonkuzhali, "A dual-band circular polarized CPW fed low-profile antenna for WLAN and X-band applications," *Results in Engineering*, Vol. 27, 106466, 2025.

[13] Jash, S. S., C. Goswami, and R. Ghatak, "A low profile broadband circularly polarized planar antenna with an embedded slot realized on a reactive impedance surface," *AEU — International Journal of Electronics and Communications*, Vol. 108, 62–72, 2019.

[14] Li, Z., Y. Liu, M. Zhao, W. Zong, and S. He, "A wideband circularly polarized metasurface antenna with high gain using characteristic mode analysis," *Electronics*, Vol. 14, No. 14, 2818, 2025.

[15] Yousef, B. M., A. M. Ameen, M. D. Alanazi, M. Rajagopal, and A. A. Ibrahim, "A wide-band antenna with circular polarization utilizing a U-shaped radiator and parasitic strip for wireless communications," *Micromachines*, Vol. 14, No. 7, 1308, 2023.

[16] Obeng Kwakye, K. S., N. Rasool, K. O. Gyasi, J. Abroquah, M. S. Ellis, O. L. Owusu, A.-R. Ahmed, and J. J. Kponyo, "Design and analysis of a low-profile dual-band circularly polarized monopole antenna based on characteristic mode analysis," *International Journal of RF and Microwave Computer-Aided Engineering*, Vol. 2023, No. 1, 7855907, 2023.

[17] Chen, Z., X. Zheng, C. Song, J. Zhang, V. Volskiy, Y. Li, and G. A. E. Vandenbosch, "Enhancing circular polarization performance of low-profile patch antennas for wearables using characteristic mode analysis," *Sensors*, Vol. 23, No. 5, 2474, 2023.

[18] Li, H., R. Zhang, L. Tian, B. Xie, Z. Zhu, and Y. Ren, "Design of low-profile broadband circularly polarized flat-top metasurface antenna," *Journal of Physics D: Applied Physics*, Vol. 58, No. 26, 265105, 2025.

[19] Nakamura, T. and T. Fukusako, "Broadband design of circularly polarized microstrip patch antenna using artificial ground structure with rectangular unit cells," *IEEE Transactions on Antennas and Propagation*, Vol. 59, No. 6, 2103–2110, 2011.

[20] Ding, C., R. Wu, and J. Dong, "Characteristic mode inspired circular polarization antenna using metamaterial," in *2021 International Applied Computational Electromagnetics Society (ACES-China) Symposium*, 1–2, Chengdu, China, 2021.

[21] Lohar, F. L., I. B. Sharma, V. Katewa, and M. M. Sharma, "T-shaped tri-band antenna based on characteristic mode analysis for satellite applications," *Progress In Electromagnetics Research C*, Vol. 115, 65–80, 2021.

[22] Sharma, I. B., F. L. Lohar, P. Joshi, J. Garg, and M. M. Sharma, "Multi-band antenna design by reshaping surface currents of higher order mode using CMA method," *IETE Journal of Research*, Vol. 70, No. 6, 5572–5582, 2024.

[23] Balanis, C. A., *Antenna Theory: Analysis and Design*, John Wiley & Sons, 2016.

[24] Chang, L., L.-L. Chen, J.-Q. Zhang, and D. Li, "A wideband circularly polarized antenna with characteristic mode analysis," *International Journal of Antennas and Propagation*, Vol. 2020, No. 1, 5379892, 2020.

[25] Lohar, F. L., C. Dhote, Y. Solunke, and N. K. Suyan, "Design of circularly polarized irnss receiver antenna using characteristic mode analysis," in *2019 IEEE Indian Conference on Antennas and Propogation (InCAP)*, 1–5, Ahmedabad, India, 2019.

[26] Yeung, S. H. and C.-F. Wang, "Study of a parasitic U-slot patch array antenna with characteristic mode analysis," *Microwave and Optical Technology Letters*, Vol. 60, No. 2, 482–488, 2018.

[27] Ayn, Q., S. Yuvaraj, and K. K. Gurrala, "Design and analysis of low-profile dual-band circularly polarized antenna using CMA for wearable applications," *Sādhanā*, Vol. 50, No. 3, 185, 2025.

[28] Dhara, R., "Design of a miniaturized CPW fed Z-shaped monopole antenna using theory of characteristics modes for bandwidth enhancement," *Sādhanā*, Vol. 46, No. 2, 87, 2021.

[29] Wu, J., Y. Yin, Z. Wang, and R. Lian, "Broadband circularly polarized patch antenna with parasitic strips," *IEEE Antennas and*

Wireless Propagation Letters, Vol. 14, 559–562, 2014.

[30] Yang, H., X. Liu, and Y. Fan, "Design of broadband circularly polarized all-textile antenna and its conformal array for wearable devices," *IEEE Transactions on Antennas and Propagation*, Vol. 70, No. 1, 209–220, 2022.

[31] Hu, X., S. Yan, J. Zhang, V. Volski, and G. A. E. Vandenbosch, "Omni-directional circularly polarized button antenna for 5 GHz WBAN applications," *IEEE Transactions on Antennas and Propagation*, Vol. 69, No. 8, 5054–5059, 2021.

[32] Mir, R., H. Dashti, and J. Ahmadi-Shokouh, "Design and analysis of circularly polarized circular patch antenna with multiple shorting pins using characteristic mode theory," *AEU — International Journal of Electronics and Communications*, Vol. 146, 154112, 2022.

[33] Jhajharia, T., V. Tiwari, D. Yadav, S. Rawat, and D. Bhatnagar, "Wideband circularly polarised antenna with an asymmetric meandered-shaped monopole and defected ground structure for wireless communication," *IET Microwaves, Antennas & Propagation*, Vol. 12, No. 9, 1554–1558, 2018.

[34] Jhajharia, T., V. Tiwari, D. Bhatnagar, D. Yadav, and S. Rawat, "A dual-band CP dual-orthogonal arms monopole antenna with slanting edge DGS for C-band wireless applications," *AEU — International Journal of Electronics and Communications*, Vol. 84, 251–257, 2018.

[35] Jhajharia, T., V. Tiwari, and D. Bhatnagar, "Polarisation reconfigurable dual-band circularly polarised patch antenna with defected ground plane for C-band wireless applications," *IET Microwaves, Antennas & Propagation*, Vol. 13, No. 14, 2551–2558, 2019.